Article

Three-dimensional atomic structure and local chemical order of medium- and high-entropy nanoalloys

Saman Moniri[1,5], Yao Yang[1,5], Jun Ding[2,5], Yakun Yuan[1], Jihan Zhou[1], Long Yang[1], Fan Zhu[1], Yuxuan Liao[1], Yonggang Yao[3], Liangbing Hu[3], Peter Ercius[4] & Jianwei Miao[1✉]

Medium- and high-entropy alloys (M/HEAs) mix several principal elements with near-equiatomic composition and represent a model-shift strategy for designing previously unknown materials in metallurgy[1–8], catalysis[9–14] and other fields[15–18]. One of the core hypotheses of M/HEAs is lattice distortion[5,19,20], which has been investigated by different numerical and experimental techniques[21–26]. However, determining the three-dimensional (3D) lattice distortion in M/HEAs remains a challenge. Moreover, the presumed random elemental mixing in M/HEAs has been questioned by X-ray and neutron studies[27], atomistic simulations[28–30], energy dispersive spectroscopy[31,32] and electron diffraction[33,34], which suggest the existence of local chemical order in M/HEAs. However, direct experimental observation of the 3D local chemical order has been difficult because energy dispersive spectroscopy integrates the composition of atomic columns along the zone axes[7,32,34] and diffuse electron reflections may originate from planar defects instead of local chemical order[35]. Here we determine the 3D atomic positions of M/HEA nanoparticles using atomic electron tomography[36] and quantitatively characterize the local lattice distortion, strain tensor, twin boundaries, dislocation cores and chemical short-range order (CSRO). We find that the high-entropy alloys have larger local lattice distortion and more heterogeneous strain than the medium-entropy alloys and that strain is correlated to CSRO. We also observe CSRO-mediated twinning in the medium-entropy alloys, that is, twinning occurs in energetically unfavoured CSRO regions but not in energetically favoured CSRO ones, which represents, to our knowledge, the first experimental observation of correlating local chemical order with structural defects in any material. We expect that this work will not only expand our fundamental understanding of this important class of materials but also provide the foundation for tailoring M/HEA properties through engineering lattice distortion and local chemical order.

Strength and ductility are two important material properties, but they are mutually exclusive in most materials[37]. Recent experiments have demonstrated that several medium- and high-entropy alloys (M/HEAs) can overcome this strength–ductility trade-off[3–8,38–40]. The high strength of M/HEAs stems from the different elemental components acting as solutes[41], local chemical order[30] and heterogeneous lattice strain[25,26], which raise the energy barrier of dislocation motion[40]. Although the dislocation glide in face-centred cubic (fcc) metals leads to high ductility with reduced strength[37], twinning in M/HEAs provides a distinct plasticity mechanism that obstructs dislocation motion and gains strength while remaining ductile[42]. This twinning-induced, simultaneous increase in strength and ductility in M/HEAs has led to both

mechanistically driven and property-discovering investigations for structural applications[3,7,38–40,43]. However, the degree and influence of atomic segregation and chemical short-range order (CSRO) on twin formation remain unclear in both M/HEAs and other alloys. Recent atomistic simulations have indicated a link between CSRO and twinning in medium-entropy alloys (MEAs)[28,30], but there is no experimental evidence.

Furthermore, CSRO, lattice distortion and surface strain strongly affect the catalytic activity of M/HEAs[9–14]. Unlike conventional catalysts, M/HEAs confine different elements to the same lattice, which distorts the lattice structure and induces strain[12,13]. The lattice distortion and surface strain along with the chemical diversity of adsorption sites

[1]Department of Physics and Astronomy and California NanoSystems Institute, University of California, Los Angeles, Los Angeles, CA, USA. [2]Center for Alloy Innovation and Design, State Key Laboratory for Mechanical Behavior of Materials, Xi'an Jiaotong University, Xi'an, China. [3]Department of Materials Science and Engineering, University of Maryland, College Park, MD, USA. [4]National Center for Electron Microscopy, Molecular Foundry, Lawrence Berkeley National Laboratory, Berkeley, CA, USA. [5]These authors contributed equally: Saman Moniri, Yao Yang, Jun Ding. ✉e-mail: j.miao@ucla.edu
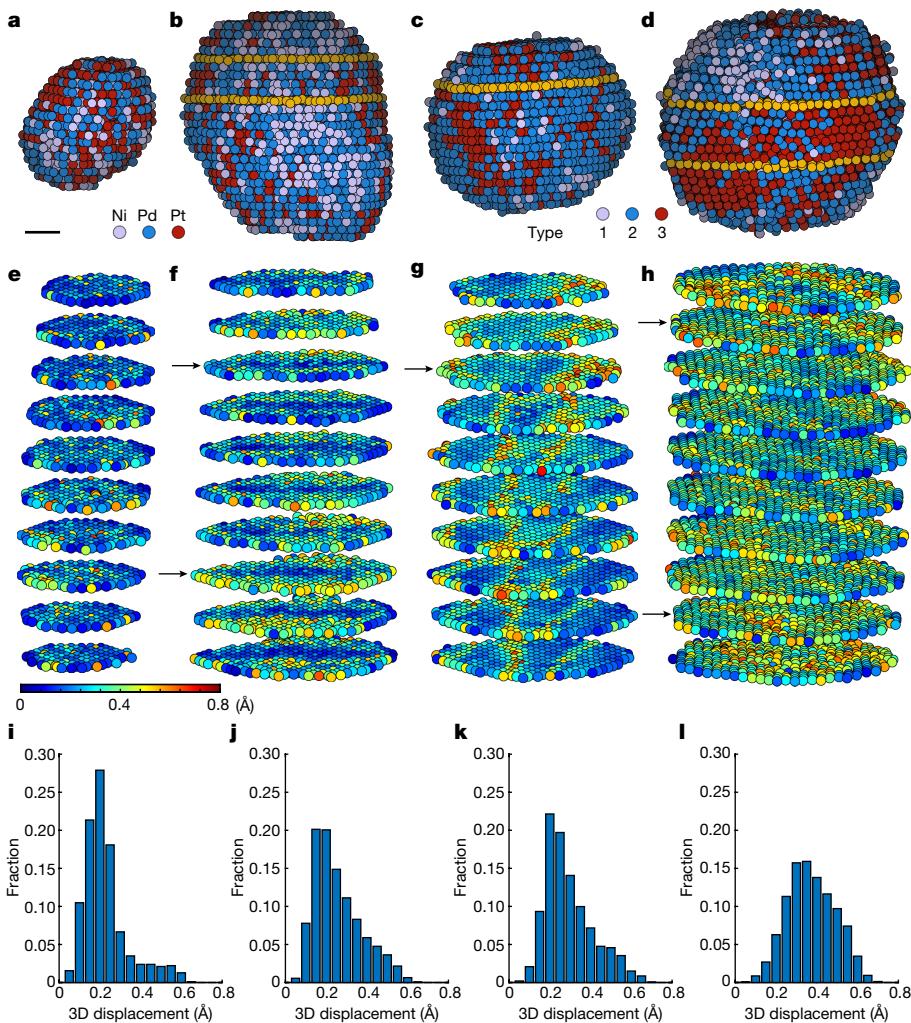
Fig. 1 | The 3D atomic structure and lattice distortion of M/HEA nanoparticles. a–d, Experimental atomic models of two MEAs and two HEAs, named MEA-1 (**a**), MEA-2 (**b**), HEA-1 (**c**) and HEA-2 (**d**), respectively, in which the yellow circles represent the atoms along the twin boundaries. Scale bar, 1 nm. **e–h**, Atomic layer-by-layer visualization of the 3D displacements of MEA-1,

MEA-2, HEA-1 and HEA-2, in which the arrows point to the twin boundaries. **i–l**, The distributions of the 3D atomic displacements of MEA-1, MEA-2, HEA-1 and HEA-2 with the mean and standard deviation as 0.23 ± 0.11 Å, 0.26 ± 0.12 Å, 0.29 ± 0.12 Å, and 0.37 ± 0.12 Å, respectively.

increase the activity, selectivity and durability of M/HEA catalysts[9,13,44–46]. However, our current understanding of the lattice distortion, strain and CSRO in M/HEA catalysts remains limited because of the dearth of three-dimensional (3D) space and atomic-scale information from diffraction, spectroscopy, electron microscopy and atomistic simulations[9–14]. Here we used atomic electron tomography (AET) to determine the 3D atomic coordinates of NiPdPt-based M/HEA nanoparticles. We quantified the 3D lattice distortion, strain tensor, dislocations, twin boundaries and CSRO of the M/HEAs at the atomic scale. We observe a correlation between strain and CSRO in the M/HEAs and a direct link between CSRO and twinning in the MEAs.

3D lattice distortion and strain tensor

We chose NiPdPt-based M/HEA nanoparticles as a model in this study as these nanoparticles are not only catalytically active[14,47–49] but also provide sufficient image contrast for AET to identify their atomic species and types[36]. The M/HEA nanoparticles were synthesized by a carbothermal shock method[50] (Methods and Extended Data Table 1), and the distribution of the eight elements in the high-entropy alloys (HEAs) was confirmed by energy dispersive spectroscopy (EDS) maps (Extended Data Fig. 1). The AET experiments were performed with a

scanning transmission electron microscope in the annular dark-field mode (Methods). Tomographic tilt series were acquired from six MEA and four HEA nanoparticles (Extended Data Table 2). These nanoparticles were stable under the electron beam by corroborating the consistency of the images taken before, during and after the data acquisition. After image pre-processing, each tilt series was reconstructed by an advanced tomographic algorithm and the 3D atomic coordinates were traced, classified and refined to produce an experimental atomic model (Methods). The experimental precision of the 3D atomic coordinates was estimated to be 19.5 pm (Extended Data Fig. 2). Although we resolved the atomic species in the MEA nanoparticles as Ni, Pd and Pt, the eight elements in the HEA nanoparticles were classified into three types (Co and Ni as type 1; Ru, Rh, Pd and Ag as type 2; Ir and Pt as type 3) because the atomic numbers of several elements differ by only one and cannot be distinguished by AET[36]. The number of atoms and the atomic species and types of the M/HEA are shown in Extended Data Table 2.

Figure 1a–d and Extended Data Fig. 3 show the experimental 3D atomic models of the 10 M/HEA nanoparticles, exhibiting a single-phase fcc structure. To quantify the local lattice distortion of the M/HEAs, we compared each atom and its nearest neighbours with a reference fcc lattice to determine the 3D atomic displacement (Methods). Figure 1e–h
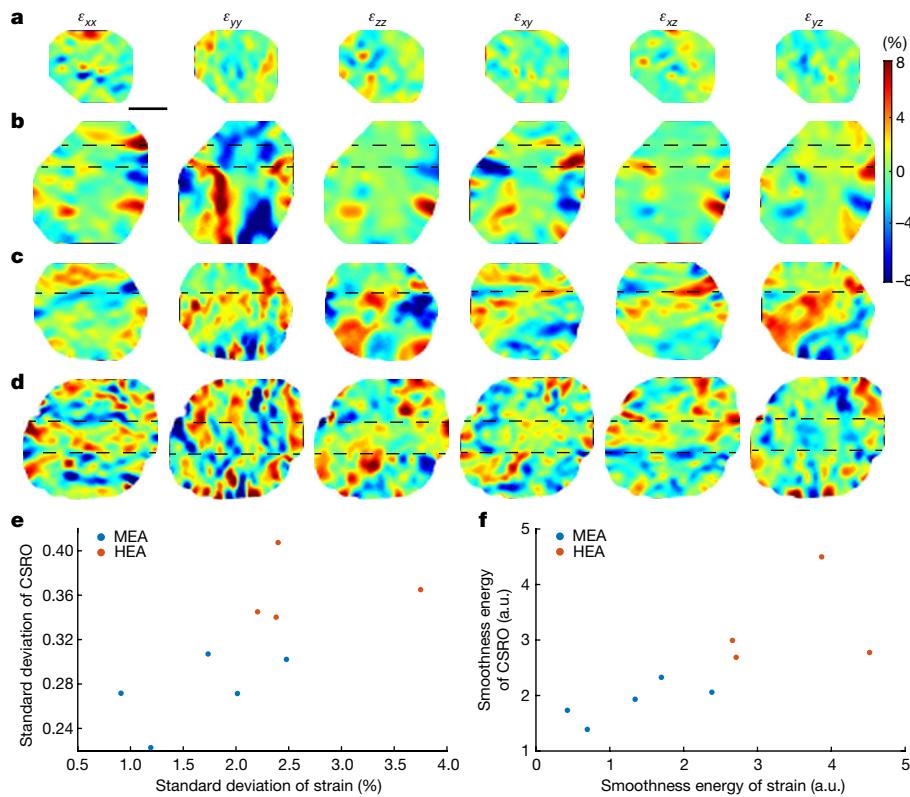
Fig. 2 | 3D strain tensor measurements of the M/HEA nanoparticles. a–d, The six components of the local strain tensor of a representative atomic layer in MEA-1 (**a**), MEA-2 (**b**), HEA-1 (**c**) and HEA-2 (**d**) along the $[1\bar{1}0]$ direction, in which the dashed lines represent the twin boundaries. Scale bar, 2 nm. **e**, Standard deviation of strain and CSRO for five MEA and four HEA nanoparticles, which quantifies the average amount of deviation from the mean. MEA-5 is excluded in the calculation because of a grain boundary (Extended Data Fig. 3c). **f**, Smoothness energy (that is, local fluctuation) of strain and CSRO for the M/HEA nanoparticles, which quantifies the local heterogeneity of strain and CSRO. a.u., arbitrary units.

shows the 3D atomic displacements of two representative MEAs and two HEAs, named MEA-1, MEA-2, HEA-1 and HEA-2, respectively. The mean and standard deviation of the atomic displacements of the four nanoparticles are 0.23 ± 0.11 Å, 0.26 ± 0.12 Å, 0.29 ± 0.12 Å and 0.37 ± 0.12 Å, respectively (Fig. 1i–l). A statistical analysis of these data shows that the HEAs have larger local lattice distortion than the MEAs (Extended Data Table 3). From the experimental 3D atomic coordinates, we also determined the local strain tensor of the M/HEAs using a method described elsewhere[51] (Methods). Figure 2 shows the six components of the local strain tensor for MEA-1, MEA-2, HEA-1 and HEA-2, in which the compressive, tensile and shear strains range from −8% to +8%. To quantify the local heterogeneity of the strain tensor, we calculated the standard deviation and the smoothness energy (Methods). The standard deviation measures the average amount of deviation from the mean, whereas the smoothness energy quantifies the local fluctuation. The larger the smoothness energy, the larger the local fluctuation. Figure 2e,f shows that the HEAs have more heterogeneous strain than the MEAs.

Next, we characterize the twins and dislocations in the M/HEAs. Among the 10 M/HEAs, 4 are twin-free, 2 have a single twin, 3 have double twins, and 1 has a grain boundary and double twins (Fig. 1a–d, Methods and Extended Data Fig. 3). The abundance of the single and double twins in M/HEAs is different from conventional nanoparticles, which have fewer twins except for decahedral multiply twinned nanoparticles[52,53]. Compared with the MEAs, the HEAs have more diffuse twin boundaries with each boundary spreading to the neighbouring atomic layers (Extended Data Fig. 4a–e). We also observe that the HEAs are more prone to having dislocations than the MEAs. Extended Data Fig. 4f–i shows the cores of three Shockley partial dislocations and two screw dislocations in the M/HEAs and the corresponding Burgers vectors.

quantifies the average amount of deviation from the mean. MEA-5 is excluded in the calculation because of a grain boundary (Extended Data Fig. 3c). **f**, Smoothness energy (that is, local fluctuation) of strain and CSRO for the M/HEA nanoparticles, which quantifies the local heterogeneity of strain and CSRO. a.u., arbitrary units.

Observation of CSRO-mediated twinning

To quantify the local chemical order in the M/HEAs, we compute the CSRO parameters (α_{ij}) between each atom and its nearest neighbours[30,54] (Methods). For pairs of the same species or types ($i = j$), a positive α_{ii} indicates a tendency to segregate, and a negative α_{ii} the opposite. For pairs of different species or types ($i \neq j$), a negative α_{ij} indicates favourable inter-mixing, and a positive α_{ij} the opposite. A quantitative analysis of CSRO and strain indicates that the HEAs have more heterogeneous CSRO than the MEAs, and that CSRO is correlated with strain in the M/HEAs (Fig. 2e,f). Figure 3a,b and Extended Data Fig. 5a–d show the 3D distribution of the six CSRO parameters (α_{NiNi}, α_{PdPd}, α_{PtPt}, α_{NiPd}, α_{NiPt} and α_{PdPt}) of twin-free MEA-1. The 3D distribution is heterogeneous with the formation of pockets of local chemical order, indicating that CSRO can propagate from the ångström scale to the nanometre scale. To quantify the local chemical order, we averaged every CSRO parameter for each atomic layer along the [111] direction (Fig. 3c,d and Extended Data Fig. 5e–h). We observe that all the average α_{NiPt} values are negative and most of the average α_{PdPt} values are positive, indicating the tendency of the inter-mixing between Ni and Pt atoms and the separation between the Pd and Pt atoms. To validate our experimental observations, we performed density functional theory (DFT)-based calculations to predict energy-favoured CSRO in a twin-free NiPdPt MEA (Methods). Figure 3i shows the histogram of the six average CSRO parameters of the twin-free MEA between the DFT calculations and experimental observations, confirming a favourable bonding between Ni and Pt atoms and an unfavourable bonding between Pd and Pt atoms in twin-free MEAs.

As a comparison, we calculated the six CSRO parameters for double-twinned MEA-2. Figure 3e,f and Extended Data Fig. 5i–l show the
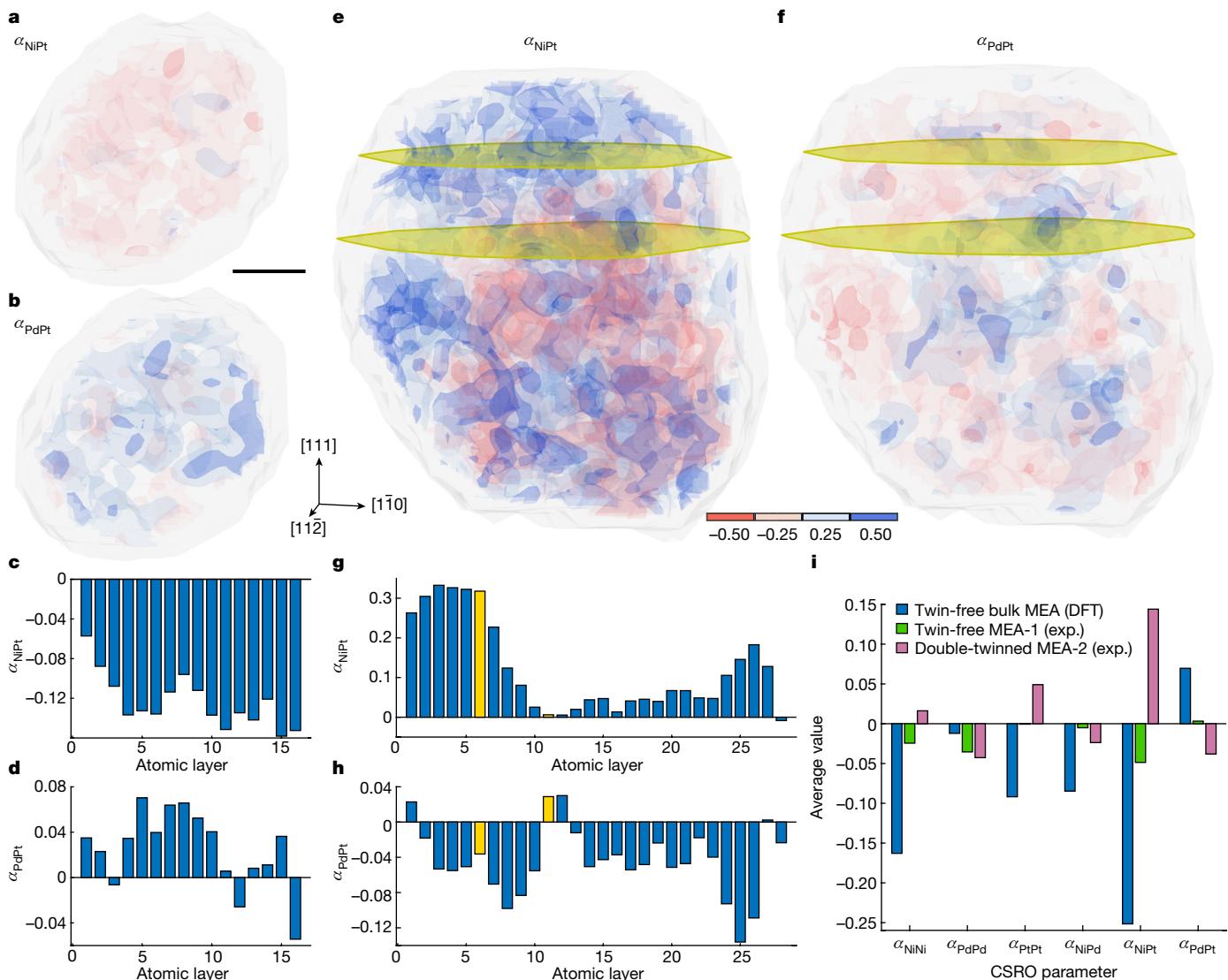
Fig. 3 | Experimental observation of the correlation between CSRO and twinning in MEAs. a,b, The 3D distribution of α_{NiPt} (**a**) and α_{PdPt} (**b**) in twin-free MEA-1. Scale bar, 1 nm. **c,d**, Histogram of the average α_{NiPt} (**c**) and α_{PdPt} (**d**) values for each atomic layer along the [111] direction, indicating the tendency of inter-mixing between the Ni and Pt atoms and the separation between the Pd and Pt atoms. **e,f**, 3D distribution of α_{NiPt} (**e**) and α_{PdPt} (**f**) in double-twinned MEA-2 (the twins marked with yellow planes), exhibiting more heterogeneous CSRO than twin-free MEA-1 (**a,b**). **g,h**, Histogram of the average α_{NiPt} (**g**) and α_{PdPt} (**h**) values for each atomic layer along the [111] direction (the yellow bars indicate the twin positions), which are the opposite of α_{NiPt} and α_{PdPt} for twin-free MEA-1 (**c,d**). **i**, Histogram of the average values for the six CSRO parameters of a DFT-calculated bulk MEA, twin-free MEA-1 and double-twinned MEA-2.

3D distribution of the six parameters, in which the yellow planes represent the twin boundaries. The CSRO parameters of the double-twinned MEA are more heterogeneous than that of the twin-free MEA. Some pockets of local chemical order are connected to each other to form elongated structures that extend over a few nanometres. Figure 3g,h and Extended Data Fig. 5m–p show the histograms of the six average CSRO parameters of each atomic layer parallel to the twin boundaries. Most of the α_{NiPt} and α_{PdPt} values are positive and negative, respectively (Fig. 3g,h), which are the opposite of α_{NiPt} and α_{PdPt} of twin-free MEA-1 (Fig. 3c,d). The average α_{NiPt} and α_{PdPt} values of the double-twinned MEA are the reverse of those of the twin-free MEA as well as the DFT calculations of a twin-free bulk MEA (Fig. 3i). These observations indicate that the separation of the favourable atomic species (Ni and Pt) and the inter-mixing of the unfavourable atomic species (Pd and Pt) facilitate the formation of the twins, which are further corroborated by the analysis of the other double-twinned MEA nanoparticle (Extended Data Fig. 6).

To investigate the impact of CSRO on the twin-formation energy (E_{TF}) of the MEAs, we used the experimental 3D atomic coordinates and

species as a direct input to molecular dynamics simulations and calculated E_{TF} as a function of the twin position (Methods). We first applied this approach to a single-twinned MEA. Figure 4a–e shows the change of E_{TF} by moving the twin from the zeroth to the tenth atomic layer along the [111] direction, in which the zeroth layer indicates twin-free MEA. Four representative atomic configurations are shown in Fig. 4a–d with the twin marked in yellow. We observe that E_{TF} changes from negative to positive when the twin is moved from atomic layers 5 to 6 (Fig. 4e). The experimentally determined twin position is in layer 5 (yellow bar), which is next to the minimum E_{TF} in layer 4. Next, we used the experimental 3D atomic coordinates of double-twinned MEA-2 as input to molecular dynamics simulations to calculate E_{TF} as a function of the twin separation. While fixing one twin, we moved the other twin layer-by-layer along the [111] direction and computed the corresponding E_{TF} (Fig. 4f–i). We find that E_{TF} changes from negative to positive between a twin separation of atomic layers 5 and 6. The experimentally determined twin separation is five atomic layers (yellow bar in Fig. 4i), which is next to the minimum E_{TF} with a twin separation of four layers. We analysed
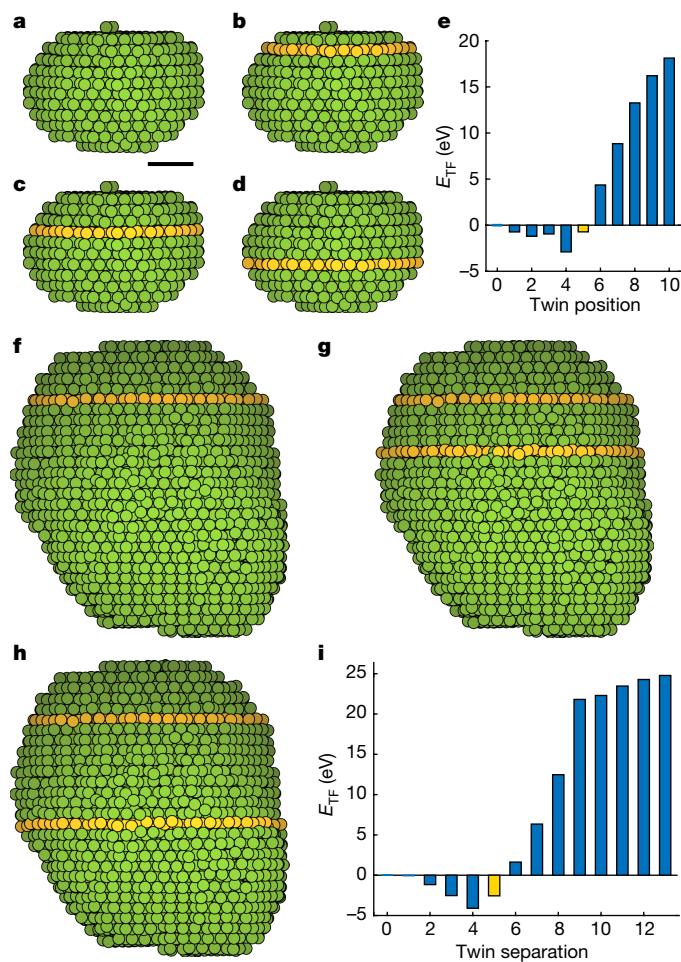
Fig. 4 | The twin-formation energy (E_{TF}) calculated from the experimental 3D atomic coordinates and species of the MEAs. a–d, Calculation of E_{TF} of a single-twinned MEA by moving the twin (yellow circles) from the zeroth (top) to the tenth atomic layer along the [111] direction, with four representative atomic configurations showing the twin in layer 0 (that is, twin-free) (**a**), layer 3 (**b**), layer 5 (**c**) and layer 8 (**d**). Scale bar, 1 nm. **e**, Histogram of E_{TF} as a function of the twin position, in which E_{TF} changes from negative to positive from atomic layers 5 to 6. The experimentally determined twin is in layer 5 (yellow bar), which is next to the minimum E_{TF} in layer 4. **f-h**, Calculation of E_{TF} of the double-twinned MEA by fixing one twin (yellow circles in **f**) and moving the other twin along the [111] direction, in which the three representative atomic configurations show a twin separation by 0 (that is, a single twin) (**f**), 5 (**g**), and 10 atomic layers (**h**). **i**, Histogram of E_{TF} as a function of the twin separation, in which E_{TF} changes from negative to positive between a twin separation of five and six layers. The experimentally determined twin separation is five atomic layers (yellow bar), which is next to the minimum E_{TF} with a twin separation of four layers.

the other double-twinned MEA nanoparticle and obtained consistent results (Extended Data Fig. 7). All these observations show a correlation between the CSRO and twinning in the MEAs, that is, energetically unfavourable CSRO lowers the E_{TF}. As the samples were synthesized by heating the metal precursors to about 2,000 K in approximately 50 ms, followed by rapid cooling at about 10^5 K s^{-1} (Methods)[50], this quenching process essentially freezes the CSRO in the molten alloy because there is not sufficient time for atomic diffusion to appreciably change the CSRO. Therefore, we conclude that the CSRO mediates the formation of twins in the MEA nanoparticles.

Compared with the MEAs, the HEAs exhibit greater local chemical fluctuation. Extended Data Figs. 8a–f and 9a–f show the 3D distribution of the six CSRO parameters for a twin-free and a double-twinned HEA,

which are more heterogeneous than those of the MEAs (Fig. 2e). The increase in the chemical complexity from the three-element MEAs to the eight-element HEAs leads to a larger distortion of the twin geometry as shown in the formation of atomic steps along the twins of both the MEAs and HEAs (Extended Data Fig. 4b–e), with the latter containing several such steps that disrupt the stacking of the neighbouring atomic planes. To examine the correlation between CSRO and twinning in the HEAs, we calculated the six average CSRO parameters of the atomic layer along the [111] direction for a twin-free HEA (Extended Data Fig. 8g–l). In comparison, the six average CSRO parameters for a double-twinned HEA are shown in Extended Data Fig. 9g–l. We observe the reverse of α_{13} between the twin-free and double-twinned HEAs, indicating that the separation of the favourable atomic types 1 and 3 facilitates the formation of the twins in the HEAs (Extended Data Fig. 9m). Because our AET experiment can classify only the eight elements in the HEAs into three types, we cannot calculate the E_{TF} from the experimental 3D atomic coordinates and types of the HEA as in the case of the MEAs.

Conclusions

Lattice distortion and CSRO are two fundamental features that strongly affect the unique properties of M/HEAs. Despite substantial insights from various studies[21–31,33,34], direct 3D structure information remains unknown. Here we overcome this limitation by advancing AET to determine the 3D atomic positions of M/HEAs and quantitatively characterize their local lattice distortion, strain tensor, dislocation cores and CSRO in three dimensions. We find a correlation between strain and CSRO in the M/HEAs. We also observe CSRO-mediated twinning in the MEAs, which confirms the DFT calculations of the NiPdPt MEA (Fig. 3i) and the atomistic simulations of the CrCoNi MEA[28,30]. Owing to the tunability of CSRO during materials manufacturing, our 3D atomic-scale insights into the correlation between CSRO and twinning could expand the horizon for the design of M/HEAs and other alloys with targeted structure–property relationships. Although we focus on M/HEA nanoparticles in this work, AET could be combined with EDS to determine the 3D atomic positions and local chemical order of bulk M/HEAs by milling them into needles or thin specimens.

Furthermore, M/HEA catalysts have shown performance enhancement over conventional alloys for various multi-step reactions[12,14], including ammonia oxidation and decomposition[9,50], carbon dioxide reduction[44,45] and methane combustion[55]. M/HEA catalysts also possess near-continuum adsorbate binding energies with greater structural stability[12,14,49]. Thus, determining the 3D atomic structure of M/HEA catalysts and measuring their 3D local lattice distortion and strain could pave the way for their rational design in a largely untapped range of compositions and structures. The present case study of NiPdPt-based M/HEA nanoparticles provides insights into the heterogeneous distribution of strain and CSRO and represents an important step in this direction. Recently, we have demonstrated that the experimental 3D atomic coordinates from AET can be used as direct input to DFT to obtain more accurate electronic properties[56] and, together with machine learning, to identify the active sites of Pt alloy nanocatalysts for the oxygen reduction reaction[57]. Immediate extension of this approach to M/HEA nanoparticles could enable the discovery of yet-unknown attributes of this emerging class of catalysts. We expect that the ability to determine the 3D atomic structure and local chemical order of M/HEAs will extend to both the pursuit of superior strength–ductility combinations of the metallurgical community and the quest towards optimized surface adsorption energies of the catalysis community.

Online content

Any methods, additional references, Nature Portfolio reporting summaries, source data, extended data, supplementary information,

1. Yeh, J.-W. et al. Nanostructured high-entropy alloys with multiple principal elements: Novel alloy design concepts and outcomes. *Adv. Eng. Mater.* **6**, 299–303 (2004).
2. Cantor, B., Chang, I. T. H., Knight, P. & Vincent, A. J. B. Microstructural development in equiatomic multicomponent alloys. *Mater. Sci. Eng. A* **375–377**, 213–218 (2004).
3. Gludovatz, B. et al. A fracture-resistant high-entropy alloy for cryogenic applications. *Science* **345**, 1153–1158 (2014).
4. Li, Z., Pradeep, K. G., Deng, Y., Raabe, D. & Tasan, C. C. Metastable high-entropy dual-phase alloys overcome the strength-ductility trade-off. *Nature* **534**, 227–230 (2016).
5. Miracle, D. B. & Senkov, O. N. A critical review of high entropy alloys and related concepts. *Acta Mater.* **122**, 448–511 (2017).
6. Yang, T. et al. Multicomponent intermetallic nanoparticles and superb mechanical behaviors of complex alloys. *Science* **362**, 933–937 (2018).
7. George, E. P., Raabe, D. & Ritchie, R. O. High-entropy alloys. *Nat. Rev. Mater.* **4**, 515–534 (2019).
8. Ren, J. et al. Strong yet ductile nanolamellar high-entropy alloys by additive manufacturing. *Nature* **608**, 62–68 (2022).
9. Xie, P. et al. Highly efficient decomposition of ammonia using high-entropy alloy catalysts. *Nat. Commun.* **10**, 4011 (2019).
10. Batchelor, T. A. A. et al. High-entropy alloys as a discovery platform for electrocatalysis. *Joule* **3**, 834–845 (2019).
11. Xin, Y. et al. High-entropy alloys as a platform for catalysis: progress, challenges, and opportunities. *ACS Catal.* **10**, 11280–11306 (2020).
12. Löffler, T., Ludwig, A., Rossmeisl, J. & Schuhmann, W. What makes high-entropy alloys exceptional electrocatalysts? *Angew. Chem. Int. Ed.* **60**, 26894–26903 (2021).
13. Sun, Y. & Dai, S. High-entropy materials for catalysis: a new frontier. *Sci. Adv.* **7**, eabg1600 (2021).
14. Yao, Y. et al. High-entropy nanoparticles: synthesis-structure-property relationships and data-driven discovery. *Science* **376**, eabn3103 (2022).
15. Koželj, P. et al. Discovery of a superconducting high-entropy alloy. *Phys. Rev. Lett.* **113**, 107001 (2014).
16. Sarkar, A. et al. High entropy oxides for reversible energy storage. *Nat. Commun.* **9**, 3400 (2018).
17. Li, W., Liu, P. & Liaw, P. K. Microstructures and properties of high-entropy alloy films and coatings: a review. *Mater. Res. Lett.* **6**, 199–229 (2018).
18. Jiang, B. et al. High figure-of-merit and power generation in high-entropy GeTe-based thermoelectrics. *Science* **377**, 208–213 (2022).
19. Tsai, M.-H. & Yeh, J.-W. High-entropy alloys: a critical review. *Mater. Res. Lett.* **2**, 107–123 (2014).
20. He, Q. & Yang, Y. On lattice distortion in high entropy alloys. *Front. Mater.* **5**, 42 (2018).
21. Zou, Y., Maiti, S., Steurer, W. & Spolenak, R. Size-dependent plasticity in an $Nb_{25}Mo_{25}Ta_{25}W_{25}$ refractory high-entropy alloy. *Acta Mater.* **65**, 85–97 (2014).
22. Owen, L. R. et al. An assessment of the lattice strain in the CrMnFeCoNi high-entropy alloy. *Acta Mater.* **122**, 11–18 (2017).
23. Song, H. et al. Local lattice distortion in high-entropy alloys. *Phys. Rev. Mater.* **1**, 023404 (2017).
24. Lee, C. et al. Lattice distortion in a strong and ductile refractory high-entropy alloy. *Acta Mater.* **160**, 158–172 (2018).
25. Li, J. et al. Heterogeneous lattice strain strengthening in severely distorted crystalline solids. *Proc. Natl Acad. Sci. USA* **119**, e2200607119 (2022).
26. Chen, B. et al. Correlating dislocation mobility with local lattice distortion in refractory multi-principal element alloys. *Scr. Mater.* **222**, 115048 (2023).
27. Zhang, F. X. et al. Local Structure and Short-Range Order in a NiCoCr Solid Solution Alloy. *Phys. Rev. Lett.* **118**, 205501 (2017).
28. Ding, J., Yu, Q., Asta, M. & Ritchie, R. O. Tunable stacking fault energies by tailoring local chemical order in CrCoNi medium-entropy alloys. *Proc. Natl Acad. Sci. USA* **115**, 8919–8924 (2018).
29. Ma, Y. et al. Chemical short-range orders and the induced structural transition in high-entropy alloys. *Scr. Mater.* **144**, 64–68 (2018).
30. Li, Q. J., Sheng, H. & Ma, E. Strengthening in multi-principal element alloys with local-chemical-order roughened dislocation pathways. *Nat. Commun.* **10**, 3563 (2019).
31. Ding, Q. et al. Tuning element distribution, structure and properties by composition in high-entropy alloys. *Nature* **574**, 223–227 (2019).
32. Zhang, R., Chen, Y., Fang, Y. & Yu, Q. Characterization of chemical local ordering and heterogeneity in high-entropy alloys. *MRS Bull.* **47**, 186–193 (2022).
33. Zhang, R. et al. Short-range order and its impact on the CrCoNi medium-entropy alloy. *Nature* **581**, 283–287 (2020).
34. Chen, X. et al. Direct observation of chemical short-range order in a medium-entropy alloy. *Nature* **592**, 712–716 (2021).
35. Walsh, F., Zhang, M., Ritchie, R. O., Minor, A. M. & Asta, M. Extra electron reflections in concentrated alloys do not necessitate short-range order. *Nat. Mater.* **22**, 926–929 (2023).
36. Miao, J., Ercius, P. & Billinge, S. J. L. Atomic electron tomography: 3D structures without crystals. *Science* **353**, aaf2157 (2016).
37. Ritchie, R. O. The conflicts between strength and toughness. *Nat. Mater.* **10**, 817–822 (2011).
38. Gludovatz, B. et al. Exceptional damage-tolerance of a medium-entropy alloy CrCoNi at cryogenic temperatures. *Nat. Commun.* **7**, 10602 (2016).
39. Zhang, Z. et al. Dislocation mechanisms and 3D twin architectures generate exceptional strength-ductility-toughness combination in CrCoNi medium-entropy alloy. *Nat. Commun.* **8**, 14390 (2017).
40. Ma, E. & Wu, X. Tailoring heterogeneities in high-entropy alloys to promote strength–ductility synergy. *Nat. Commun.* **10**, 5623 (2019).
41. Varvenne, C., Luque, A. & Curtin, W. A. Theory of strengthening in fcc high entropy alloys. *Acta Mater.* **118**, 164–176 (2016).
42. Lu, K., Lu, L. & Suresh, S. Strengthening materials by engineering coherent internal boundaries at the nanoscale. *Science* **324**, 349–352 (2009).
43. Otto, F. et al. The influences of temperature and microstructure on the tensile properties of a CoCrFeMnNi high-entropy alloy. *Acta Mater.* **61**, 5743–5755 (2013).
44. Pedersen, J. K., Batchelor, T. A. A., Bagger, A. & Rossmeisl, J. High-entropy alloys as catalysts for the CO_2 and CO reduction reactions. *ACS Catal.* **10**, 2169–2176 (2020).
45. Nellaiappan, S. et al. High-entropy alloys as catalysts for the CO_2 and CO reduction reactions: experimental realization. *ACS Catal.* **10**, 3658–3663 (2020).
46. Pedersen, J. K. et al. Bayesian optimization of high-entropy alloy compositions for electrocatalytic oxygen reduction. *Angew. Chem. Int. Ed.* **60**, 24144–24152 (2021).
47. Xie, S. et al. Atomic layer-by-layer deposition of Pt on Pd nanocubes for catalysts with enhanced activity and durability toward oxygen reduction. *Nano Lett.* **14**, 3570–3576 (2014).
48. Cruz-Martínez, H. et al. NiPdPt trimetallic nanoparticles as efficient electrocatalysts towards the oxygen reduction reaction. *Int. J. Hydrogen Energy* **44**, 12463–12469 (2019).
49. Wu, D. et al. Noble-metal high-entropy-alloy nanoparticles: atomic-level insight into the electronic structure. *J. Am. Chem. Soc.* **144**, 3365–3369 (2022).
50. Yao, Y. et al. Carbothermal shock synthesis of high-entropy-alloy nanoparticles. *Science* **359**, 1489–1494 (2018).
51. Xu, R. et al. Three-dimensional coordinates of individual atoms in materials revealed by electron tomography. *Nat. Mater.* **14**, 1099–1103 (2015).
52. Chen, C.-C. et al. Three-dimensional imaging of dislocations in a nanoparticle at atomic resolution. *Nature* **496**, 74–77 (2013).
53. Johnson, C. L. J. et al. Effects of elastic anisotropy on strain distributions in decahedral gold nanoparticles. *Nature Mater.* **7**, 120–124 (2008).
54. De Fontaine, D. The number of independent pair-correlation functions in multicomponent systems. *J. Appl. Crystallogr.* **4**, 15–19 (1971).
55. Li, T. et al. Denary oxide nanoparticles as highly stable catalysts for methane combustion. *Nat. Catal.* **4**, 62–70 (2021).
56. Tian, X. et al. Correlating the three-dimensional atomic defects and electronic properties of two-dimensional transition metal dichalcogenides. *Nat. Mater.* **19**, 867–873 (2020).
57. Yang, Y. et al. Atomic-scale identification of the active sites of nanocatalysts. Preprint at https://arxiv.org/abs/2202.09460 (2023).

Article

Methods

Sample synthesis

The M/HEA samples were prepared by a carbothermal shock method[50]. Metal precursors in ethanol (0.05 M) were mixed into the desired multi-element composition (Extended Data Table 1) and dipped onto a carbon heater for Joule heating, in which reduced graphene oxide was used as the substrate for dispersion and stabilization. After drying at room temperature, metal precursors on the reduced graphene oxide were rapidly heated to a high temperature (about 2,000 K for approximately 50 ms) by Joule heating followed by rapid cooling (about 10^5 K s^{-1}). This sample synthesis procedure enabled us to fully mix various elements into M/HEA nanoparticles[14,50].

AET data acquisition

The AET experiments of 10 M/HEA nanoparticles were performed using the TEAM 0.5 microscope with the TEAM stage at the National Center for Electron Microscopy, with the scanning transmission electron microscope operated in the annular dark-field (ADF-STEM) mode at 200 kV or 300 kV (Extended Data Table 2). At each tilt angle, a nearby nanoparticle or a sample feature was used as a fiducial to align and focus the image, thereby reducing the unnecessary exposure of the region of interest to the electron beam[58]. To minimize the drift distortion and electron dose at each tilt angle, three to four sequential images were taken with a dwell time of 3 μs. The total electron dose of each tilt series was optimized to be between 4.7×10^5 e$^-$ Å^{-2} and 1.1×10^6 e$^-$ Å^{-2} to reduce the beam damage (Extended Data Table 2). For each sample, we confirmed the structural stability on beam exposure by comparing images before, during and after the acquisition of the tilt series.

Image pre-processing

A multi-step image pre-processing protocol was performed on each AET dataset as outlined below.

1. Drift correction: To compensate for sample drift during data acquisition, we collected three to four images at each tilt angle, computed the cross-correlation coefficient between the images and identified the relative drift vectors by the maximum cross-correlation. We used a step size of 0.1 pixels as the drift in typical ADF-STEM images is smaller than 1 pixel. We applied the drift correction to each image along the slow scan direction and corrected for it by interpolating the raw images with drift-corrected pixel positions. The drift-corrected images were then averaged to form a single image at each tilt angle.

2. Image denoising: To remove the Poisson and Gaussian noise from the drift-corrected images, we used the block-matching and 3D filtering algorithm[59], which has been successfully used to denoise experimental AET datasets[60,61]. To optimize the block-matching and 3D filtering denoising parameters for each dataset, we first estimated the level of each noise type (Poisson and Gaussian) in the image stack. Then, these noise levels were added to several simulated ADF-STEM images of model nanoparticles with similar size and elemental distribution as the experimental data. The denoising parameters leading to the maximum cross-correlation between the simulated images and the experimental images were applied to the experimental data.

3. Background subtraction: For each denoised image, we used Otsu thresholding in MATLAB to generate a mask of the nanoparticle, which is slightly larger than its boundary. Using the background outside the masked region, we performed a Laplacian interpolation to estimate the background level inside the masked zone and subtracted it from the denoised image[60].

4. Image alignment: The background-subtracted images were aligned by the common line method along the tilt axis and the centre of mass method perpendicular to the tilt axis, which can align experimental tilt series with a sub-pixel accuracy[52,58].

Tomographic reconstruction

Each pre-processed dataset was reconstructed by the Real Space Iterative Reconstruction (RESIRE) algorithm[62]. RESIRE iteratively minimizes the difference between the experimental and calculated images of a sample using gradient descent. RESIRE is superior to other tomographic reconstruction algorithms by incorporating angular refinement and spatial alignment[62]. A typical RESIRE reconstruction converges after about 200 iterations. Following an initial reconstruction and an iterative process of angular refinement and spatial alignment, the background of the new set of images was re-evaluated and re-subtracted. The resulting images, after undergoing further angular refinement and spatial realignment, were used to generate the final 3D reconstruction by RESIRE.

Determining the 3D atomic coordinates and species or types

From the final 3D reconstructions, we determined the 3D atomic coordinates and species or types using the following steps.

1. Each reconstruction underwent spline interpolation by a factor of 3 to produce a finer grid, from which all the local maxima were identified. Using a polynomial fitting method[60], we identified the positions of all the peaks (that is, potential atoms) from a 0.8 Å × 0.8 Å × 0.8 Å volume around each peak. An initial list of the potential atoms was obtained by searching through all the fit peak positions with the constraint that the minimum distance between neighbouring peaks is 2 Å, given that all the interatomic distances in our samples are larger than this value.

2. To remove the non-atoms from this list, we performed K-means clustering of the integrated intensity of the local volume around each potential atom position[63,64].

3. By overlaying the 3D atomic positions with the 3D reconstructions, we manually checked the atomic positions and corrected a small fraction (<1%) of unidentified or misidentified atoms. This manual correction is routine for atom tracing and refinement in macromolecular crystallography[65].

4. The distribution of the integrated intensity of each atom is affected by several factors, including the atomic number, the electron probe size, the inner and outer angles of the detector, sample drift, angular errors, the missing wedge and noise. To accurately classify the Ni, Pd and Pt atoms in MEAs and the three types of atom in HEAs, we used K-means clustering[63,64], which has been demonstrated as a robust method to obtain consistent results from different independent runs[60,66].

5. We performed a local reclassification of all the atomic species or types. Each atom was defined to be at the centre of a sphere of radius 10 Å. The average intensity distribution of the three atomic species or types was computed within this sphere. We then computed the L_2 norm of the intensity distribution between the central atom and the average Ni, Pd and Pt or type-1, -2 and -3 atoms. The atom was assigned to the species or type with the smallest L_2 norm. After repeating this step for all the atoms, an initial experimental 3D atomic model of the sample was obtained.

6. The 3D atomic coordinates of the initial model were refined by minimizing the error between the experimental and calculated images using a gradient descent as described elsewhere[64]. The convergence of the iterative process was verified by monitoring the L_2 norm error.

Local lattice distortion and strain tensor measurements

The local lattice distortion is defined as the deviation of the experimental atomic positions in the M/HEA nanoparticles from those in a perfect fcc lattice. For each atom, its local lattice distortion (Δd_i) was calculated by

$$\Delta d_i = \frac{1}{N} \sum_j |\mathbf{r}_{ji} - \mathbf{r}_{ji}^0| \tag{1}$$

where N is the number of the nearest neighbours of atom i, $\mathbf{r}_{ji}$ is the experimental 3D coordinates of the jth nearest-neighbour atom, and $\mathbf{r}_{ji}^0$ is the perfect fcc lattice structure that is aligned to $\mathbf{r}_{ji}$ based on the three Euler angles determined by a breadth-first search algorithm[60]. A cutoff of a quarter of the nearest-neighbour bond length was applied to eliminate the contribution from some surface atoms with a large deviation. The strain tensor measurements follow a procedure described elsewhere[51]. Briefly, the atomic displacements were calculated from the measured atomic positions and a perfect fcc lattice structure. The atomic displacements were convolved with a 2-Å-wide 3D Gaussian kernel to increase the signal-to-noise ratio and precision, but reduce the 3D resolution to about 4 Å. The strain tensor was obtained by numerical differentiation of the 3D atomic displacements, in which a mask was applied to remove the edge effect[51].

The CSRO parameters
After identifying the nearest neighbours of each atom, we computed the CSRO parameters (α_{ij}) between the central atom (i) and its nearest neighbours (j) by[30,54]

$$\alpha_{ij} = \frac{p_{ij} - C_j}{\delta_{ij} - C_j} \qquad (2)$$

where p_{ij} denotes the average probability that a j-type atom is the nearest neighbour to an i-type atom, c_j indicates the average concentration of j-type atoms and δ_{ij} is the Kronecker delta function. To eliminate the boundary effect, we removed the surface atoms of each M/HEA nanoparticle from the calculation of the CSRO parameters. Following this procedure, we computed the six CSRO parameters, which are bounded between −1 and +1, for every atom in the M/HEA nanoparticles. To obtain a local CSRO distribution such as those in Fig. 3 and Extended Data Figs. 5, 6, 8 and 9, we interpolated the CSRO parameters onto 3D grids and convolved them with a Gaussian kernel. The width of the Gaussian kernel was determined by the first valley of the pair distribution function of the nanoparticle, corresponding to the first nearest-neighbour shell distance.

The twin order parameter
From the experimental 3D atomic coordinates, we fit the nearest-neighbour atoms around each atom to a perfect fcc and hexagonal close-packed (hcp) lattice by the breadth-first search algorithm[60]. If a nearest-neighbour atom has a deviation larger than a cutoff of 0.75 Å, we set its deviation to be the cutoff value. This step was to eliminate the effect of some surface atoms with a large deviation. The twin order parameter (η) was calculated by[67]

$$\eta = \frac{d_{fcc} - d_{hcp}}{d_{max}} \qquad (3)$$

where $\eta = 1$ and -1 represent the hcp and fcc structures, respectively, d_{fcc} and d_{hcp} are the sum of the deviation of the nearest-neighbour atoms from a perfect fcc lattice and hcp lattice, respectively, and d_{max} is the maximum deviation. In this study, we also calculated η using different cutoff values and obtained consistent results. With η, we can identify intrinsic and extrinsic stacking faults and twin boundaries by calculating the separation between two hcp layers: 0 for intrinsic stacking faults, 1 for extrinsic stacking faults and at least 2 for twin boundaries. In our experimental data, the separation between two hcp layers is at least 2, indicating that these are twin boundaries instead of intrinsic or extrinsic stacking faults.

Correlation between strain tensor and CSRO
To quantify the local heterogeneity of the strain tensor and CSRO, we calculated the standard deviation and the smoothness energy[68]. The standard deviation (σ) of strain or CSRO quantifies the average amount of deviation from the mean, defined as

$$\sigma = \sqrt{\frac{1}{6} \sum_{\beta} \sigma_{\beta}^2} \qquad (4)$$

where σ_{β} is the standard deviation of component β of the strain tensor or CSRO. The smoothness energy (S_E) is defined as[68]

$$S_E = \frac{1}{6N} \sum_{n,i,\beta} (\Delta_i f_{\beta}^n)^2 \qquad (5)$$

where f_{β}^n is component β of the strain tensor or CSRO, n is the nth voxel of a volume containing N voxels and Δ_i is the ith component of Laplacian with i equal to x, y or z. S_E averages the square of the second derivative of the local strain tensor or CSRO and quantifies the local fluctuation in each dataset. Larger S_E means larger local fluctuation (that is, more heterogeneous). Figure 2e,f shows the standard deviation and the smoothness energy of the strain tensor and CSRO for the M/HEA nanoparticles, in which a mask was applied to remove the edge effect. This quantitative analysis shows that (1) the HEAs have more heterogeneous strain and CSRO than the MEAs and (2) strain is correlated to CSRO in the M/HEAs.

DFT calculations
DFT-based lattice Monte Carlo approach[28] was used to show the characteristic CSRO for the NiPdPt MEA and NiCoRuRhPdAgIrPt HEA. The 256-atom configurations were generated as a special quasi-random structure[69]. The Monte Carlo simulations were run for 3,000 steps, corresponding to about 12 swap trials per atom, at a Monte Carlo temperature of 600 K. Energy calculations were performed using the Vienna ab initio simulation package[70,71]. A plane wave cutoff energy was chosen at 380 eV, and the Brillouin zone integrations were performed using Monkhorst–Pack meshes[71] with a single k-point (Γ). Projector augmented wave potentials[72] with the Perdew–Burke–Ernzerhof generalized-gradient approximation[73] were adopted for the exchange-correlation functional. From the DFT results, the lattice distortion parameter[23] was calculated as 0.089 Å and 0.11 Å for the NiPtPd MEA and NiCoRuRhPdAgIrPt HEA, respectively, which confirm our experimental observations (Fig. 1i–l).

Twin-formation energy of the MEAs
We calculated the twin-formation energy of the NiPdPt MEAs from the experimentally measured 3D atomic coordinates using the LAMMPS software package[74] with the empirical embedded-atom method potential[75]. The experimental 3D atomic coordinates of the MEA nanoparticles were obtained from the AET experiments. To eliminate the boundary effect, the surface atoms of each MEA nanoparticle were not used in the molecular dynamics calculations. For the supercell, the shrink-wrapped non-periodic boundary conditions were imposed along all three directions. As shown in Fig. 4 and Extended Data Fig. 7, the migration of the twin boundary was carried out by gradually shifting the close-packed (111) atomic planes along the ⟨112⟩ direction by the Burgers vector of the Shockley partial $b_s = \frac{a}{6}\langle11\bar{2}\rangle$. For the twin boundary at different positions, the twin-formation energy was calculated by the energy difference between the twinned and twin-free configurations after energy minimization.

Data availability
All the raw and processed experimental data are available on GitHub (https://github.com/AET-MEA-HEA/Supplementary-Data-Codes).

Code availability
All the MATLAB source codes for the 3D reconstruction, atom tracing and data analysis of this paper are available on GitHub (https://github.com/AET-MEA-HEA/Supplementary-Data-Codes).

Article

58. Scott, M. C. et al. Electron tomography at 2.4-ångström resolution. *Nature* **483**, 444–447 (2012).

59. Dabov, K., Foi, A., Katkovnik, V. & Egiazarian, K. Image denoising by sparse 3-D transform-domain collaborative filtering. *IEEE Trans. Image Process.* **16**, 2080–2095 (2007).

60. Yang, Y. et al. Determining the three-dimensional atomic structure of an amorphous solid. *Nature* **592**, 60–64 (2021).

61. Yuan, Y. et al. Three-dimensional atomic packing in amorphous solids with liquid-like structure. *Nat. Mater.* **21**, 95–102 (2022).

62. Pham, M., Yuan, Y., Rana, A., Osher, S. & Miao, J. Accurate real space iterative reconstruction (RESIRE) algorithm for tomography. *Sci. Rep.* **13**, 5624 (2023).

63. Lloyd, S. Least squares quantization in PCM. *IEEE Trans. Inf. Theory* **28**, 129–137 (1982).

64. Yang, Y. et al. Deciphering chemical order/disorder and material properties at the single-atom level. *Nature* **542**, 75–79 (2017).

65. Brünger, A. T. et al. Crystallography & NMR system: a new software suite for macromolecular structure determination. *Acta Crystallogr. D* **54**, 905–921 (1998).

66. Zhou, J. et al. Observing crystal nucleation in four dimensions using atomic electron tomography. *Nature* **570**, 500–503 (2019).

67. Pelz, P. M. et al. Simultaneous successive twinning captured by atomic electron tomography. *ACS Nano* **16**, 588–596 (2022).

68. Stein, O., Jacobson, A., Wardetzky, M. & Grinspun, E. A smoothness energy without boundary distortion for curved surfaces. *ACM Trans. Graph.* **39**, 18 (2020).

69. Zunger, A., Wei, S., Ferreira, L. G. & Bernard, J. E. Special quasirandom structures. *Phys. Rev. Lett.* **65**, 353–356 (1990).

70. Krexner, G. & Hafner, J. *Ab initio* molecular-dynamics simulation of the liquid-metal–amorphous-semiconductor transition in germanium. *Phys. Rev. B* **49**, 14251–14269 (1994).

71. Monkhorst, H. J. & Pack, J. D. Special points for Brillouin-zone integrations. *Phys. Rev. B* **13**, 5188–5192 (1976).

72. Kresse, G. & Joubert, D. From ultrasoft pseudopotentials to the projector augmented-wave method. *Phys. Rev. B* **59**, 1758–1775 (1999).

73. Perdew, J. P., Burke, K. & Ernzerhof, M. Generalized gradient approximation made simple. *Phys. Rev. Lett.* **77**, 3865–3868 (1996).

74. Plimpton, S. Fast parallel algorithms for short-range molecular dynamics. *J. Comput. Phys.* **117**, 1–19 (1995).

75. Zhou, X. W., Johnson, R. A. & Wadley, H. N. G. Misfit-energy-increasing dislocations in vapor-deposited CoFe/NiFe multilayers. *Phys. Rev. B* **69**, 144113 (2004).

Author contributions J.M. initiated and directed the project; Y. Yao and L.H. synthesized the samples; J.Z., P.E. and J.M. discussed and/or carried out the AET experiments; Y. Yang, Y. Yuan, S.M. and J.M. performed image reconstruction, atom tracing and classification for the AET experiments. S.M., Y. Yang, Y. Yuan, L.Y., F.Z., Y.L., J.D. and J.M. analysed the data and interpreted the results; J.D. performed the DFT calculations and molecular dynamics simulations with input from S.M., Y. Yang, Y. Yuan and J.M.; J.M., S.M. and Y. Yang wrote the paper. All authors commented on the paper.
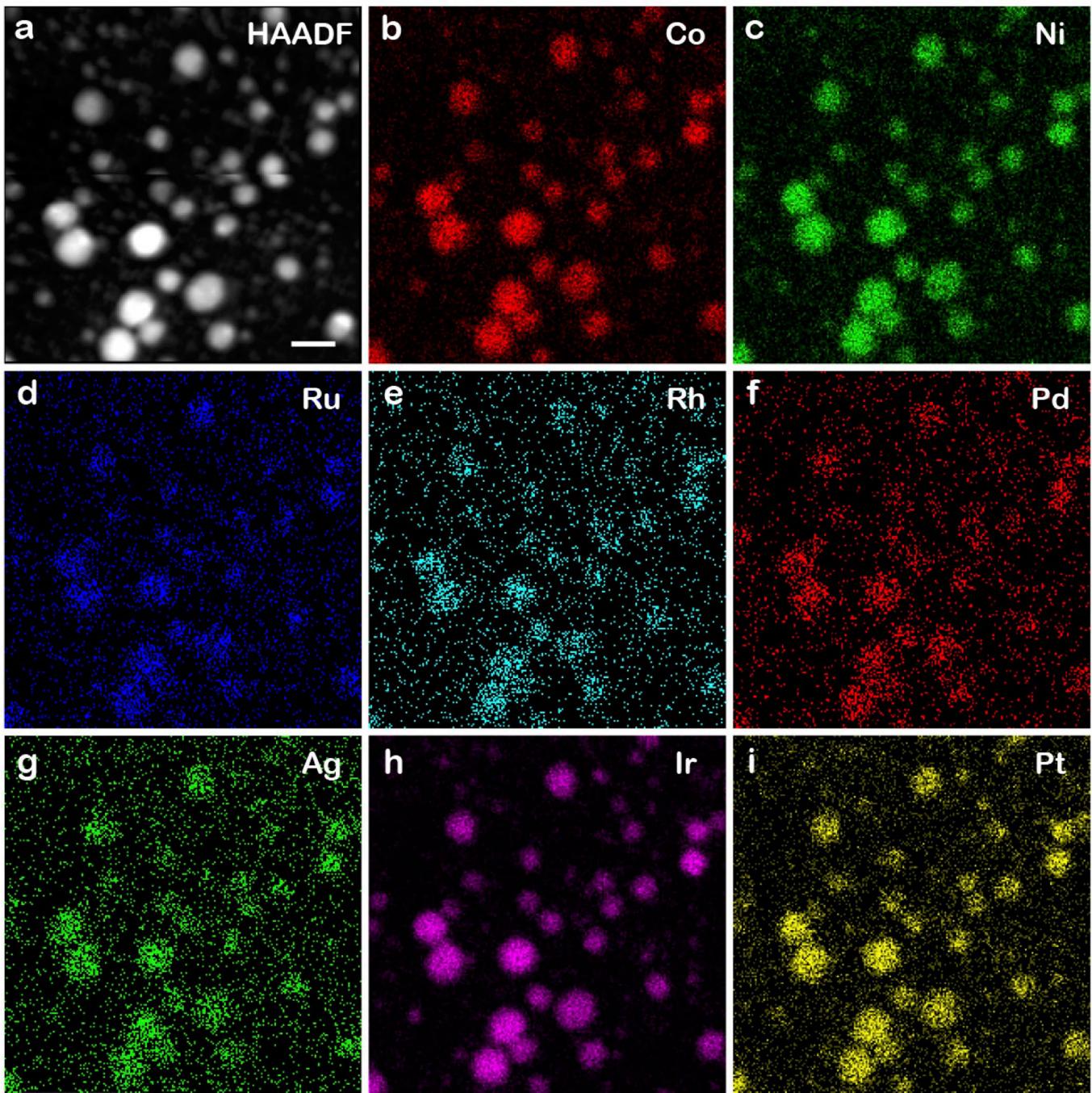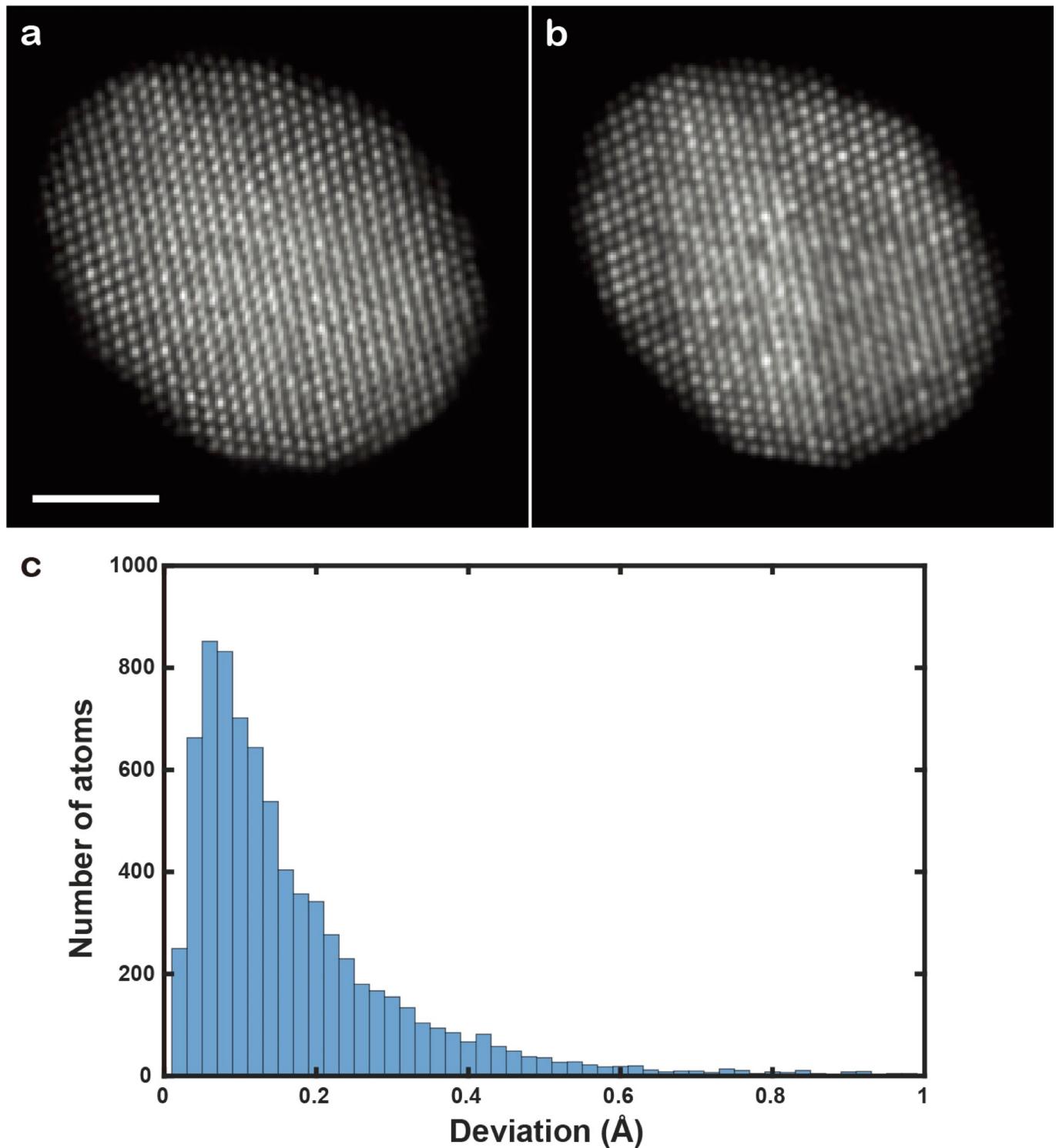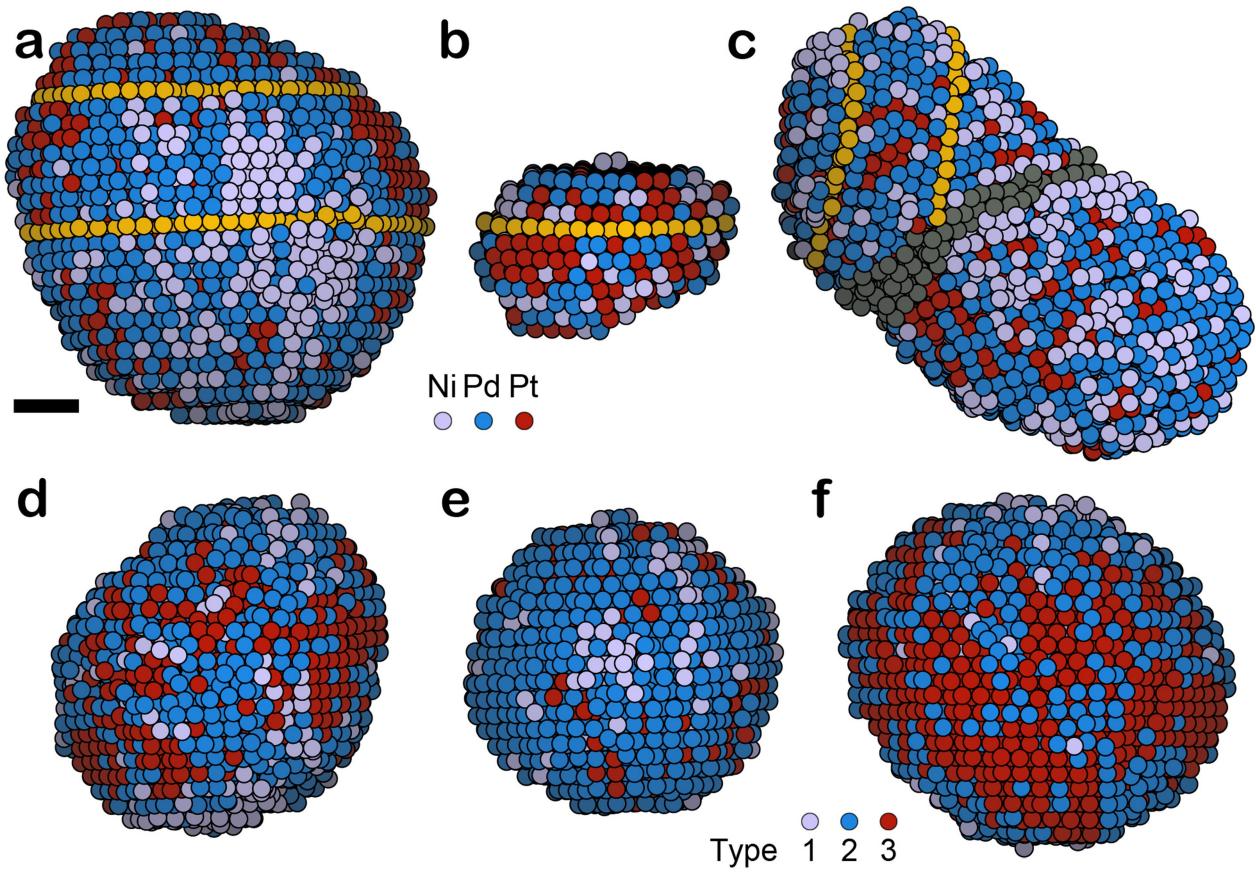
Extended Data Fig. 1 | EDS maps of the HEA nanoparticles. a, Low-resolution ADF-STEM image of the nanoparticles. Scale bars, 20 nm. **b-i**, EDS maps showing the distribution of Co (b), Ni (c), Ru (d), Rh (e), Pd (f), Ag (g), Ir (h) and Pt (i) in the nanoparticles.
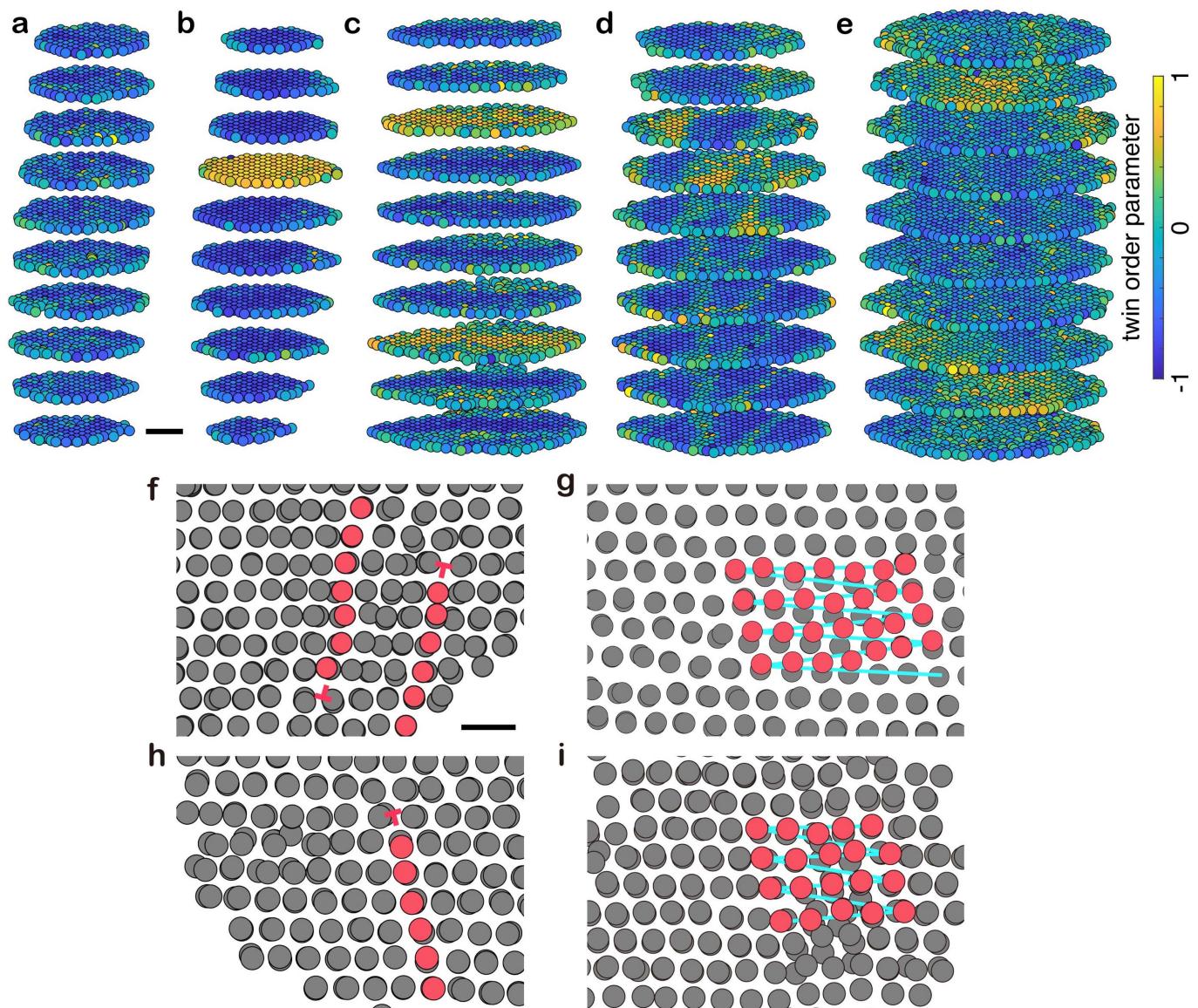
Extended Data Fig. 2 | 3D precision estimation. a, **b**, Comparison between a representative experimental (after denoising) (**a**) and a multi-slice calculated image (**b**) of MEA-3. The multi-slice images were convolved with a Gaussian function to match the incoherence effects in the experimental images. Scale bar, 2 nm. **c**, Histogram of the deviation of the 3D atomic positions between the experimental atomic model and that obtained from 55 multi-slice images. The root-mean-square deviation of the histogram is 19.5 pm.
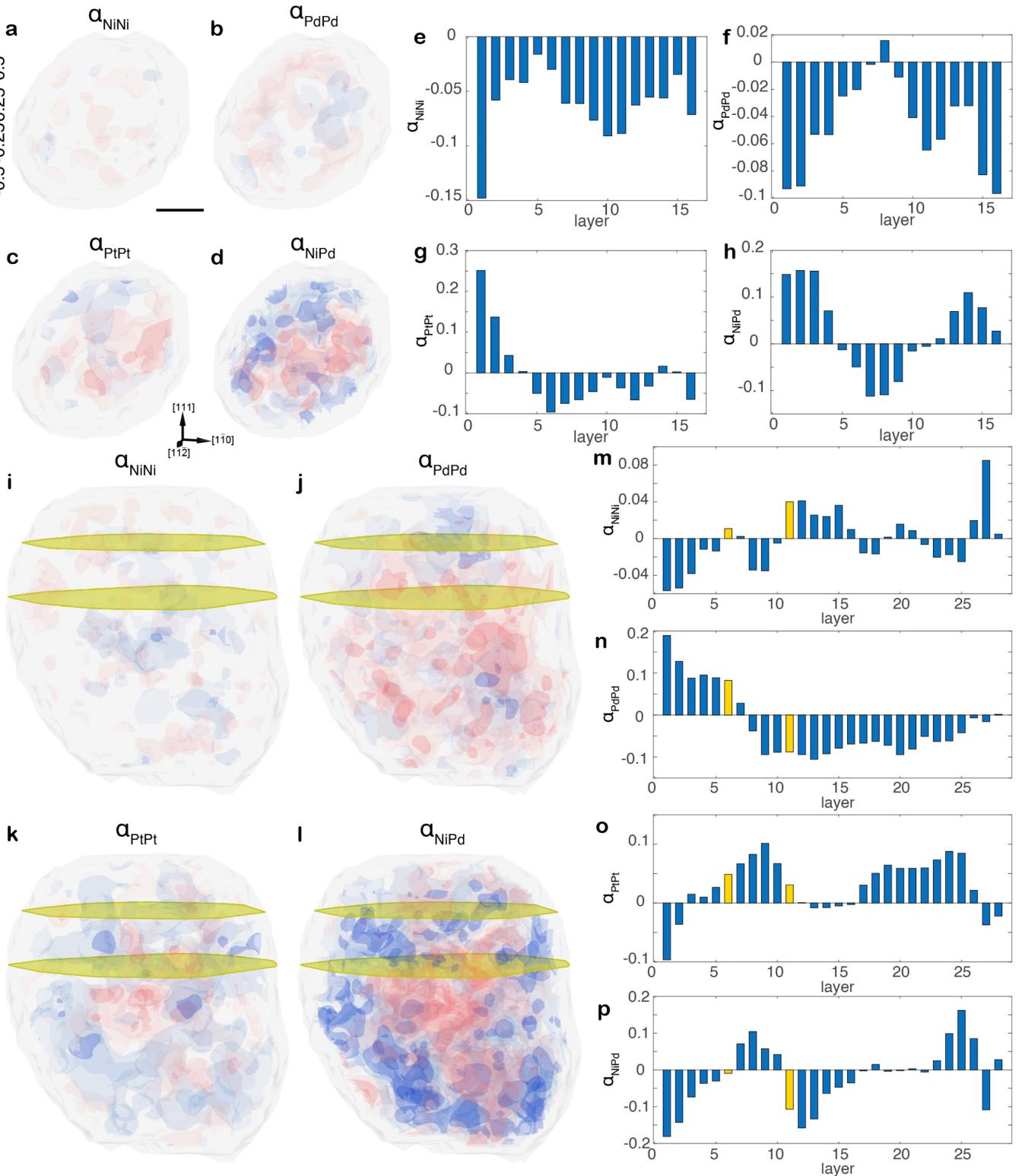
Extended Data Fig. 3 | Experimental 3D atomic models of the other six M/HEA nanoparticles. a-f, Experimental atomic models of four MEAs and two HEAs, named MEA-3 (**a**), MEA-4 (**b**), MEA-5 (**c**), MEA-6 (**d**), HEA-3 (**e**) and HEA-4 (**f**), in which the yellow circles represent the atoms along the twin boundaries in (**a-c**) and grey circles indicate the atoms on the grain boundary in (**c**). Scale bar, 1 nm.
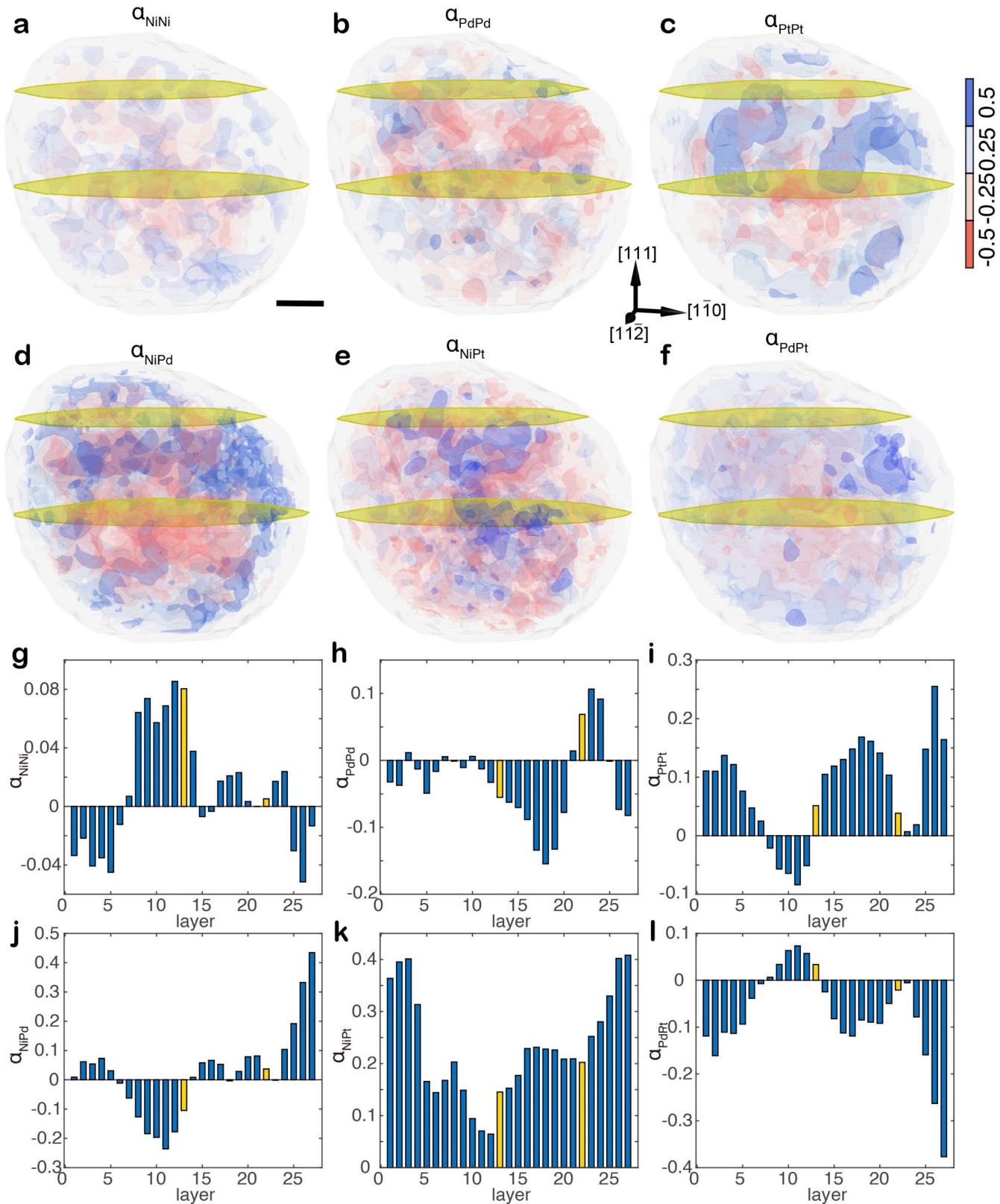
Extended Data Fig. 4 | Twin boundaries and dislocations in the M/HEAs.
a-e, The twin boundaries of three representative MEAs (**a**, twin-free; **b**, single twin; **c**, double twins) and two HEAs (**d**, single twin; **e**, double twins), showing more diffuse twin boundaries in the HEAs with each boundary spreading to the neighbouring atomic layers. The twin order parameter of 1 and −1 represents a hcp (i.e., twinning) and fcc structure, respectively. **f**, Two Shockley partial dislocations in MEA-5 with opposite Burgers vectors $\frac{a}{6}$[121] and $\frac{a}{6}$[$\bar{1}2\bar{1}$], as the gliding process was frozen near the boundary during the rapid cooling process of the nanoparticle. **g**, A screw dislocation in MEA-2 with the Burgers vector $\frac{a}{2}$[110], where the zigzag lines in light blue show the characteristic feature of the screw dislocation. **h**, A Shockley partial dislocation in HEA-4 with the Burgers vector $\frac{a}{6}$[121], which exists near the boundary of the nanoparticle. **i**, A screw dislocation in HEA-3 with the Burgers vector $\frac{a}{2}$[110]. Scale bars, 1 nm (**a**); and 5 Å (**f**).
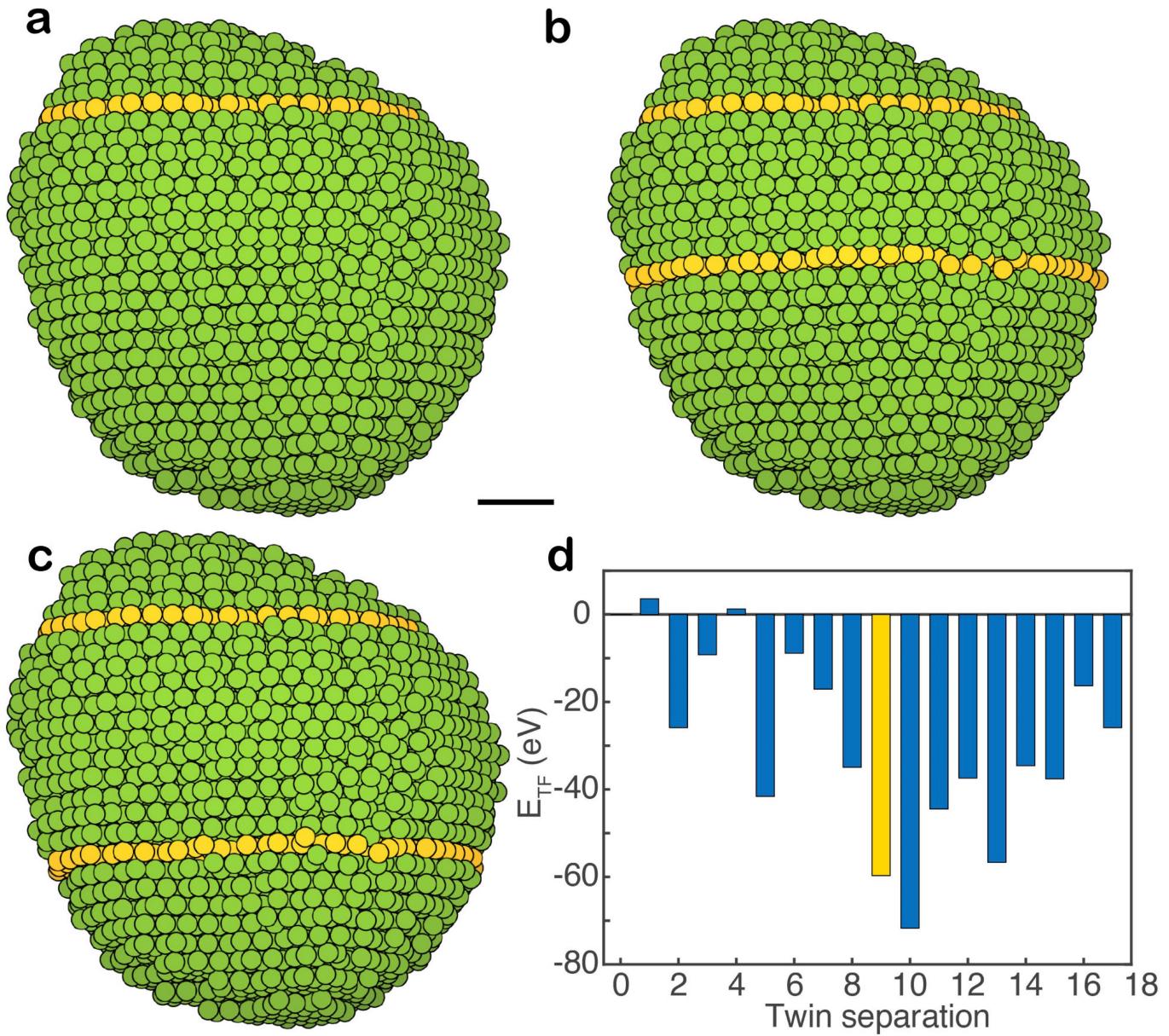
Extended Data Fig. 5 | 3D distribution of the other four CSRO parameters of twin-free MEA-1 and double-twinned MEA-2. a-d, 3D distribution of α_{NiNi}, α_{PdPd}, α_{PtPt}, and α_{NiPd} in MEA-1, showing the formation of local chemical-order pockets. **e-h**, Histogram of the average α_{NiNi}, α_{PdPd}, α_{PtPt}, and α_{NiPd} values for each atomic layer along the [111] direction in MEA-1. **i-l**, 3D distribution of α_{NiNi}, α_{PdPd}, α_{PtPt}, and α_{NiPd} in MEA-2 (the twins labelled as yellow planes), exhibiting more heterogeneous CSRO than twin-free MEA-1 (**a-d**). **m-p**, Histogram of the average α_{NiNi}, α_{PdPd}, α_{PtPt}, and α_{NiPd} values for each atomic layer along the [111] direction in MEA-2. Scale bar, 1 nm.
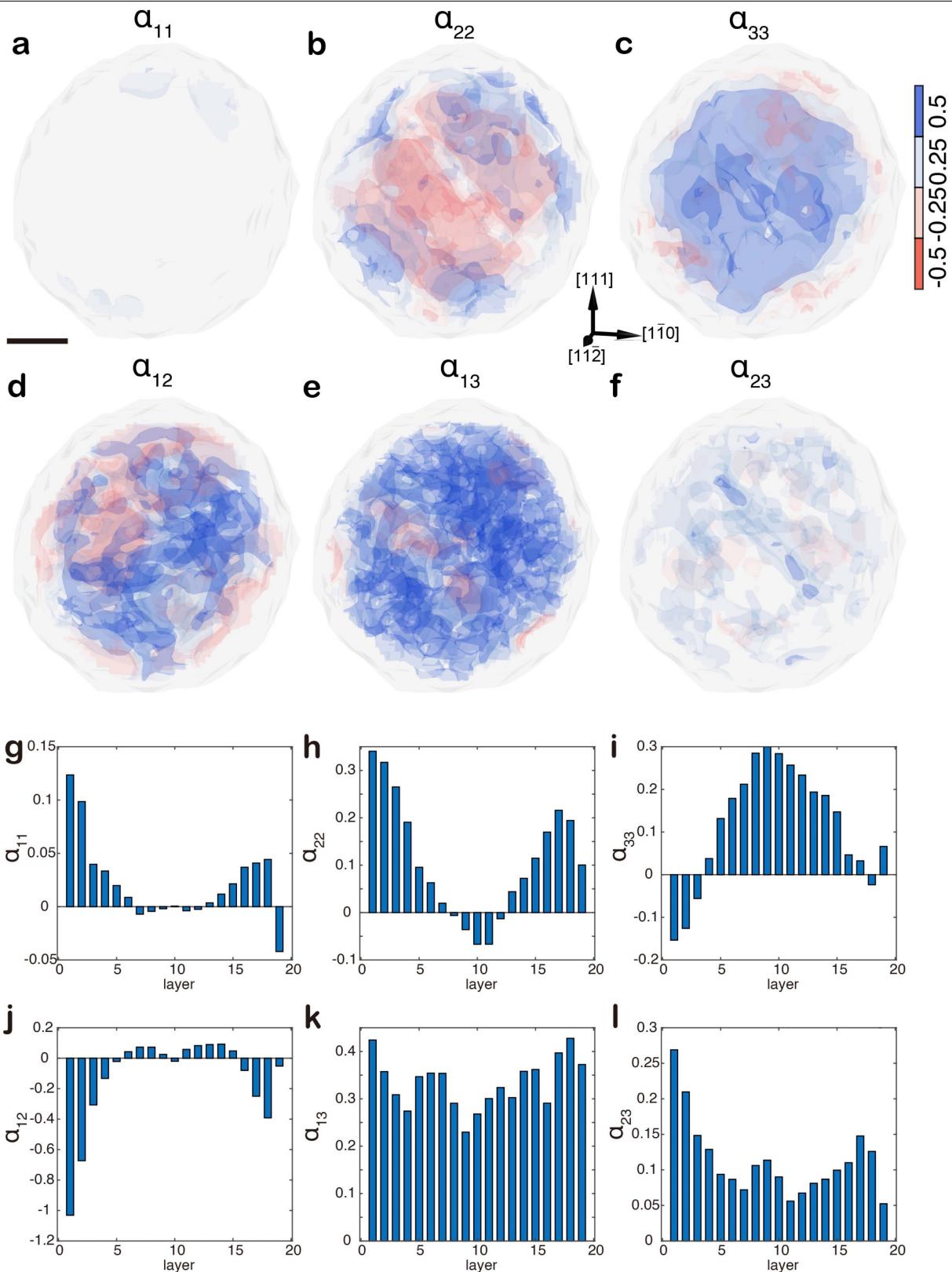
Extended Data Fig. 6 | 3D distribution of the six CSRO parameters in double-twinned MEA-3. a-f, 3D distribution of α_{NiNi}, α_{PdPd}, α_{PtPt}, α_{NiPd}, α_{NiPt}, and α_{PdPt}, where the twins are labelled as yellow planes. **g-l**, Histogram of the average α_{NiNi}, α_{PdPd}, α_{PtPt}, α_{NiPd}, α_{NiPt}, and α_{PdPt} values for each atomic layer along the [111] direction, where the yellow bars indicate the twin positions. Scale bar, 1 nm.

Extended Data Fig. 7 | Twin formation energy (E$_{TF}$) calculated from experimental 3D atomic coordinates of double-twinned MEA-3.
a-c, Calculation of E$_{TF}$ of the double-twinned MEA by fixing one twin (top yellow circles) and moving the other twin along the [111] direction, in which the three representative atomic configurations show a twin separation by 0 (i.e., a single twin) (**a**), 9 (**b**), and 13 atomic layers (**c**). **d**, Histogram of E$_{TF}$ as a function of the twin separation. The experimentally determined twin separation is 9 atomic layers (yellow bar), which is next to the minimum E$_{TF}$ with a twin separation of 10 layers. Scale bar, 1 nm.
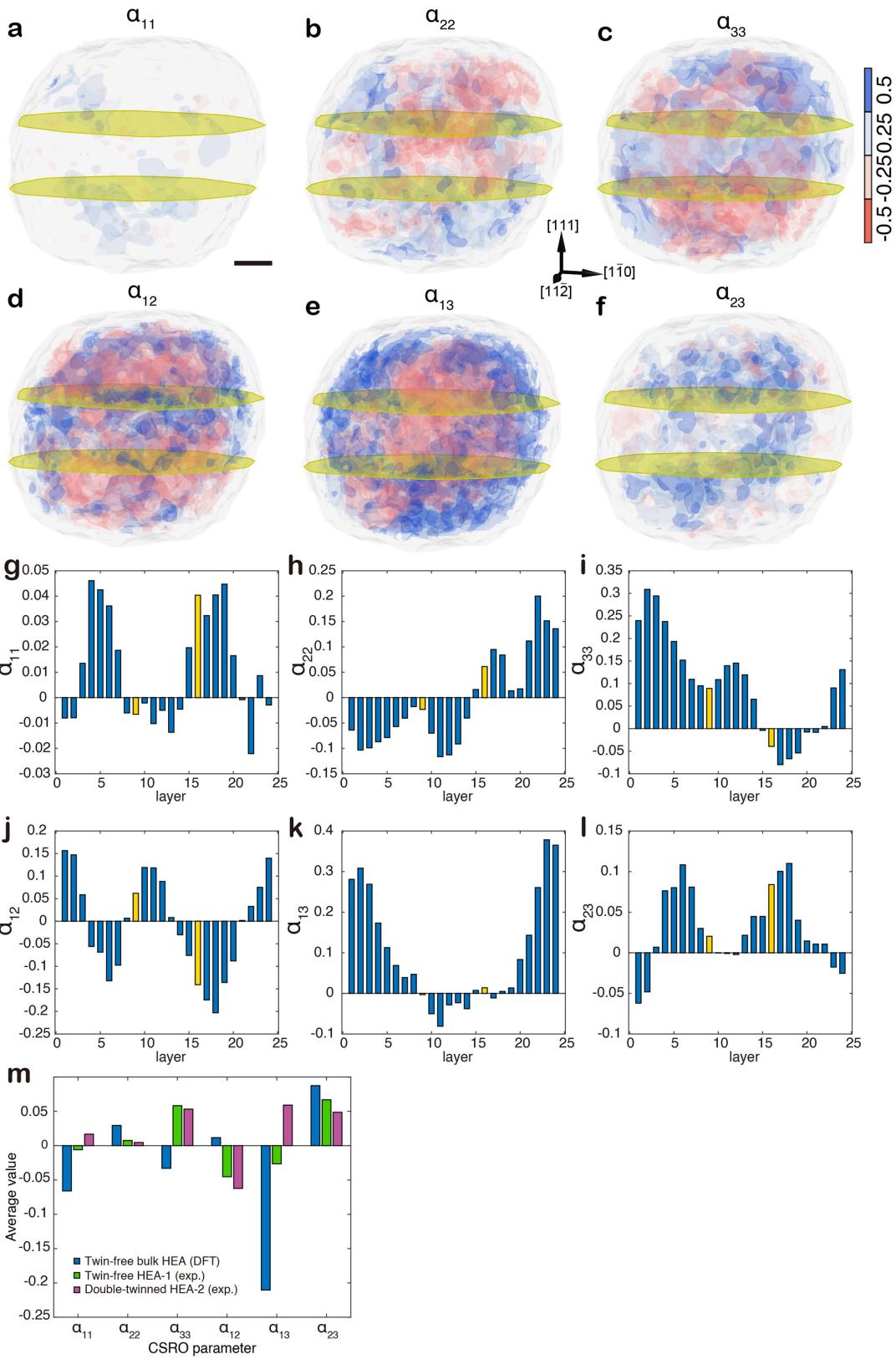
Extended Data Fig. 8 | 3D distribution of the six CSRO parameters in twin-free HEA-1. a-f, 3D distribution of α_{11}, α_{22}, α_{33}, α_{12}, α_{13}, and α_{23}, which are more heterogeneous than those of the twin-free MEAs (Fig. 3a,b, Extended Data Fig. 5a–d). **g-l**, Histograms of the average α_{11}, α_{22}, α_{33}, α_{12}, α_{13}, and α_{23} values for the atomic layer along the [111] direction. Scale bar, 1 nm.

Extended Data Fig. 9 | 3D distribution of the six CSRO parameters in double-twinned HEA-2. a-f, 3D distribution of α_{11}, α_{22}, α_{33}, α_{12}, α_{13}, and α_{23}, exhibiting greater local chemical fluctuations than the double-twinned MEA (Fig. 3e,f, Extended Data Figs. 5i–l and 6a–f). **g-l**, Histograms of the average α_{11}, α_{22}, α_{33}, α_{12}, α_{13}, and α_{23} values of the atomic layer along the [111] direction. **m**, Histogram of the average values for the six CSRO parameters of a DFT-calculated bulk HEA, twin-free HEA-1, and double-twinned HEA-2. Scale bar, 1 nm.

Extended Data Table 1 | Metal precursors used for the synthesis of M/HEA nanoparticles

Salt	Solvent	Concentration	Samples
$NiCl_2 \cdot 6H_2O$	Ethanol	0.05 mol/L	
$PdCl_2$	Ethanol/ ~10 vol% 0.1M HCl	0.05 mol/L	1:1 mixture to form NiPdPt
$H_2PtCl_6 \cdot 6H_2O$	Ethanol	0.05 mol/L	
$CoCl_2 \cdot 6H_2O$	Ethanol	0.05 mol/L	
$RuCl_3 \cdot xH_2O$	Ethanol	0.05 mol/L	1:1 mixture to form CoNiRuRhPdAgIrPt
$RhCl_3 \cdot xH_2O$	Ethanol	0.05 mol/L	
$IrCl_3 \cdot xH_2O$	Ethanol	0.05 mol/L	
$AgNO_3$[*]	Ethanol	0.05 mol/L	

[*]Note the $AgNO_3$ precursor solution was dipped onto the carbon substrate after the other precursors were dipped and dried, to avoid aggregation of AgCl in the precursor solution.

Metal precursors in ethanol were mixed into the desired multielement composition, dipped onto carbon heater for Joule heating and followed by rapid cooling.

Extended Data Table 2 | AET data collection, processing, reconstruction, refinement and statistics of the ten M/HEA nanoparticles

	MEA-1[a]	MEA-2[a]	MEA3	MEA-4	MEA5	MEA-6	HEA-1[a]	HEA-2[a]	HEA-3	HEA-4
Data collection and processing										
Voltage (kV)	200	300	300	200	300	200	200	200	200	200
Convergence semi-angle (mrad)	25	30	30	25	30	25	25	25	25	25
Probe size (Å)	0.8	0.8	0.8	0.8	0.8	0.8	0.8	0.8	0.8	0.8
Detector inner angle (mrad)	38	38	38	38	38	38	38	38	38	38
Detector outer angle (mrad)	190	190	190	190	190	190	190	190	190	190
Depth of focus (nm)	8	8	8	8	8	8	8	8	8	8
Pixel size (Å)	0.347	0.434	0.434	0.347	0.306	0.347	0.347	0.347	0.347	0.347
# of images	47	55	53	57	51	59	56	54	51	56
# of frames/angle	3	3	3	3	3	4	3	3	4	3
Tilt range (°)	-55.8°	-58.5°	-58.5°	-64.7°	-58.1°	-64.7°	-66.6°	-69.6°	-69.3°	-72.0°
	63.5°	62.2°	62.2°	75.1°	62.0°	75.1°	75.8°	74.0°	63.4°	72.0°
Total electron dose (10^5 e$^-$ Å^{-2})	6.6	4.9	4.7	8.0	9.2	11.0	7.8	7.6	9.5	7.8
Reconstruction										
Algorithm	RESIRE	RESIRE	RESIRE	RESIRE	RESIRE	RESIRE	RESIRE	RESIRE	RESIRE	RESIRE
Oversampling ratio	4	4	4	4	4	4	4	4	4	4
Number of iterations	200	200	200	200	200	200	200	200	200	200
Refinement										
R_1 (%)[b]	10.10	10.29	13.68	12.00	11.43	10.03	7.90	8.46	9.95	8.21
R (%)[c]	8.38	6.89	10.17	10.23	9.05	7.05	5.60	5.89	6.48	5.84
B' factors (Å^2)										
Ni / Type 1	42.30	38.82	33.11	29.04	54.51	42.34	41.63	45.77	33.95	35.5
Pd / Type 2	37.95	28.47	25.68	29.74	37.46	37.87	37.62	46.41	32.81	34.5
Pt / Type 3	29.95	22.88	24.55	25.29	30.65	26.97	36.33	40.92	29.86	34.6
Statistics										
# of atoms										
Total	2436	8349	8141	1794	5099	5323	5672	10053	3696	6037
Ni / Type 1	989	2522	2399	545	1741	1514	1124	2638	872	1446
Pd / Type 2	597	3247	3476	430	2010	1799	2356	3830	1735	2045
Pt / Type 3	850	2580	2266	819	1348	2010	2192	3585	1089	2546

[a]MEA-1, MEA-2, HEA-1 and HEA-2 are the four nanoparticles shown in the main-text figures.
[b]The R_1-factor is defined as equation 5 in ref. 64.
[c]The R-factor is defined in equation 4 in ref. 60.

Article

Extended Data Table 3 | Unpaired t-test on the 3D atomic displacements of MEA-1, MEA-2, HEA-1 and HEA-2

P-value of unpaired t-test				
X \ Y	MEA-1	MEA-2	HEA-1	HEA-2
MEA-1	0.5	1	1	1
MEA-2	0	0.5	1	1
HEA-1	0	0	0.5	1
HEA-2	0	0	0	0.5
Test decision of unpaired t-test based on the 5% significance level				
X \ Y	MEA-1	MEA-2	HEA-1	HEA-2
MEA-1	Accept	Accept	Accept	Accept
MEA-2	Reject	Accept	Accept	Accept
HEA-1	Reject	Reject	Accept	Accept
HEA-2	Reject	Reject	Reject	Accept

Our null hypothesis is that the mean of X is not greater than that of Y, where X and Y are shown in the Table. Based on the P-value of unpaired t-test, we conclude that the mean (μ) follows this order: $\mu_{\text{MEA-1}} < \mu_{\text{MEA-2}} < \mu_{\text{HEA-1}} < \mu_{\text{HEA-2}}$.